

# Feature Resolved Turbulent Simulations over Realistic Superhydrophobic Surfaces

K. Alamé<sup>1</sup>, Y. Li<sup>1</sup>, and K. Mahesh<sup>1</sup>

(<sup>1</sup>Department of Aerospace Engineering & Mechanics, University of Minnesota, USA)

## ABSTRACT

Direct numerical simulations are performed for a turbulent channel flow at  $Re_\tau = 180$ , where  $\tau$  is the shear stress at the wall. The bottom wall is a realistically rough surface and the top wall is smooth. The volume-of-fluid methodology (VOF) is used to resolve the air-water interface, whereby the interface is considered to be flat. The height of the interface  $h$  is varied. An analytic study using multiphase unsteady Stokes approximation is performed on idealized geometry to study the damping effect of surface roughness. The main objective of the present work is to understand the effect of geometry of realistically rough surfaces on the flow in fully wetted regimes, analyze the flow statistics in the turbulent flow to study the interaction between the interface and roughness, and model the effect of unsteadiness in the viscous sublayer using a multiphase unsteady Stokes solution. Based on the results, there exists a competing effect between the interface and the rough wall. The interface suppresses vertical fluctuations whereas the exposed asperities enhance them. The unsteady Stokes flow shows that the high frequencies inhibit the transfer of forcing to the surface.

## INTRODUCTION

Superhydrophobic surfaces (SHS) have the capability to entrap gas pockets within their microtexture when submerged in water. Assuming the interface can withstand the high shear rate and unsteadiness present in the viscous sublayer of a turbulent boundary layer, the low viscosity of air in contact with fluid has the potential to reduce viscous friction between the two. This is known as the Cassie-Baxter state (Cassie and Baxter, 1944). Numerically, the roughness is commonly idealized as regular arrays of riblets, grooves, posts, or synthetic rough textures. In general the SHSs are considered to be simple grooved geometries, and numerically the interface is typically assumed to be flat and represented using zero-shear boundary conditions. Realistically,

rough surfaces do not generally have a regular pattern. Others have included the effect of viscosity on the interface (Vinogradova, 1995; Belyaev and Vinogradova, 2010; Nizkaya et al., 2014). Several papers have investigated the effect of the curvature due to the meniscus and modified the analytical solutions to take curvature into account (Cottin-Bizonne et al., 2003; Sbragaglia and Prosperetti, 2007; Wang et al., 2014; Li et al., 2017). SHS is been shown to achieve drag reduction (Ou et al., 2004; Ou and Rothstein, 2005; Joseph et al., 2006; Choi and Kim, 2006; Maynes et al., 2007; Woolford et al., 2009; Emami et al., 2011). Analytical models relate the slip lengths to various surface parameters such as groove width, pitch and height (Lauga and Stone, 2003; Ybert et al., 2007) or the slip velocities to geometry (Seo and Mani, 2016).

To the best of our knowledge, none of the past numerical work has simulated a multiphase flow over realistically rough surfaces as done in this paper. The main objective of this study is to understand the effect of geometry of realistically rough surfaces on the flow in fully wetted regimes, study the interaction between the interface and the geometry roughness and its effect on turbulent flows, model the effect of unsteadiness in the viscous sublayer of a turbulent channel using a multiphase unsteady Stokes solution. First, the effect of geometry is studied by simulating the wetted (Wenzel state (Wenzel, 1936)). Second, the multiphase aspect of the problem is investigated by modeling the two phases directly with the Volume-of-Fluid (VOF) methodology. Last, an analytical study is performed to inspect the damping effect of the surface roughness.

This paper is organized as follows: the next section outlines the numerical details of the DNS followed by the analytical model description of the unsteady multiphase Stokes solution. Then a section on computational setup presents the surface statistics of the realistic rough wall and provides a problem description of the simulation setup is given for the range of parameters considered. Results are presented in the following section

starting with a turbulent channel and concluding with a parametric study of the unsteady multiphase Stokes flow.

## SIMULATION DETAILS

### Numerical method

The governing Navier-Stokes equations of an incompressible flow are solved using the finite volume algorithm developed by Mahesh et al. (2004). The momentum and continuity equations are given by the following:

$$\frac{\partial u_i}{\partial t} + \frac{\partial}{\partial x_j}(u_i u_j) = -\frac{1}{\rho} \frac{\partial p}{\partial x_i} + \frac{1}{\rho} \frac{\partial}{\partial x_j} \left[ \mu \left( \frac{\partial u_i}{\partial x_j} + \frac{\partial u_j}{\partial x_i} \right) \right] + F_{st,i} + \delta_{i1} K_i, \quad (1)$$

$$\frac{\partial u_i}{\partial x_i} = 0, \quad (2)$$

where  $u_i$  and  $x_i$  are the  $i$ -th component of the velocity and position vectors respectively,  $p$  denotes pressure,  $\rho$  is density and  $\mu$  the viscosity of the fluid. The fluids are assumed to be immiscible. Additionally in eq. 1,  $\delta_{i1}$  is the Kroenecker delta,  $K_i$  is the body force which is only active in the liquid phase and  $F_{st,i}$  is the surface tension force. Direct numerical simulations (DNS) are performed using a mass conserving VOF methodology on structured grids to study the multiphase effect over a realistically rough surface. The algorithm is robust and emphasizes discrete kinetic energy conservation in the inviscid limit which enables it to simulate high-Reynolds number flows without adding numerical dissipation. The solution is advanced in time using a second order Adams-Bashforth method. A predictor-corrector methodology is used. The velocities are first predicted from the momentum equation and the pressure is determined from the Poisson equation. The pressure gradients are then computed and the velocity is updated to satisfy the continuity equation in the corrector step. The Poisson equation is solved using a multigrid pre-conditioned conjugate gradient method (CGM) using the Trilinos libraries (Sandia National Labs). A Crank-Nicholson discretization is used for the implicit time advancement with a linearization of the convection terms.

The volume fraction is represented by a color function ( $c$ ) to keep track of two different fluid with a range of  $0 < c < 1$  where one is a filled cell and zero in an empty cell, with an intermediate value between zero and one to define an interface cell. The volume of each fluid cell is tracked by the reconstruction and advection steps. The reconstruction step is based on a set of analytic relations proposed by Scardovelli and Zaleski (2000); given the volume fraction in each cell, the reconstruction of the interface shape uses a local normal vector

and a piecewise linear interface calculation (PLIC) to approximate the interface shape. This step geometrically conserves the volume in each cell and therefore conserves mass and prevents over- and under-shoots in the value of the color function. This ensures boundedness. The color function is then advected by the fluid velocity field, while geometrically conserving the area using a directionally split flux scheme to exchange the reference phase volume across the boundary of neighboring cells. The governing equations for the color function are given by

$$\frac{\partial c}{\partial t} + u_j \frac{\partial c}{\partial x_j} = 0, \quad (3)$$

and the density and viscosity are evaluated as

$$\rho = \rho_2 + (\rho_1 - \rho_2)c, \quad (4)$$

$$\mu = \mu_2 + (\mu_1 - \mu_2)c. \quad (5)$$

The surface tension force is modeled as a continuum surface force as proposed by Brackbill et al. (1992):

$$F_{st,i} = \sigma \kappa \frac{\partial c}{\partial x_i}, \quad (6)$$

where  $\sigma$  is the surface tension constant, and  $\kappa$  is the curvature calculated using the height function which has been shown to significantly reduce numerical errors that are associated with surface tension. These errors are known as spurious currents (Cummins et al., 2005). The gradient of the color function,  $\frac{\partial c}{\partial x_i}$ , is representative of the surface normals. The gradient term in the surface tension force is discretized in the same manner as the pressure gradient term in the projection step:

$$\Delta t \sum_f \frac{\partial p}{\partial N} A_f = \sum_f \hat{v}_N A_f + \Delta t \sigma \kappa \sum_f \frac{\partial c}{\partial N} A_f, \quad (7)$$

where  $N$  denotes the outward normal of the face with respect to the control volume on which the summation is performed. This method of discretization ensures proper pressure jump recovery across the interface. The surface is represented by obstacle cells where they are masked out from the fluid domain. The cell-centered velocities satisfy a no-slip boundary condition, with the exception of corner cells that take a weighted average of the neighboring cell-centered values. All face normal velocities are set to zero. The algorithm has been validated for a variety of flows and most recently in the context of superhydrophobicity (Li et al., 2016, 2017). In this study, we enforce a zero face-normal velocity at the interface  $\hat{v}_N|_{interface} = 0$ . The condition models a high surface tension regime with a stable flat interface, which was done to isolate the effect of varying interface heights  $h$ , given a stable finite viscosity lubricant. The assumption made is valid for flow regimes where the interfacial surface tension dominates the interface dynamics. Surface tension effects will likely become important at larger Reynolds

number flows. The statistics of the turbulent channel flow were averaged over a period of 300 flow through times after the discharge had reached a steady state value.

Given the fact that the roughness in our simulations is within the viscous sublayer, and the fact that the flow is fairly quiescent near the rough wall, we developed an analytical model based on a Stokes flow assumption to model the near wall flow field. In order to reduce the complexity of the problem, idealized longitudinal grooves are used. The analytical model is used to conduct a parametric study by varying the geometry of the groove, the interface location and the frequency of the velocity fluctuations.

### Analytical model

The turbulent flow over a rough surface with an air-water interface is modeled analytically as an unsteady multiphase Stokes flow over an idealized grooved surface where the governing equation is given by:

$$\frac{\partial u}{\partial t} = \frac{\nu}{L^2 \omega} \left( \frac{\partial^2 u}{\partial z^2} + \frac{\partial^2 u}{\partial y^2} \right). \quad (8)$$

The characteristic length scale is half periodicity of the groove  $L$ ; the velocity scale is  $L\tau/\nu$ ; the time scale is  $1/\omega$ . The solution is decomposed by  $\hat{u} = \Re(\hat{u} \exp(it)) = \Re(Y(y)Z(z) \exp(it))$ . The domain decomposition and domain definition can be seen in figure 1.

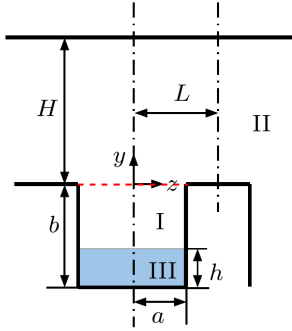


Figure 1: Model problem definition.

The general solution in each region has the form:

$$\hat{u}_I(y, z) = \sum_{n=1}^{\infty} \cos(\alpha_n z) \left\{ A_{1n} \exp \left[ \sqrt{\alpha_n^2 + \frac{iL^2 \omega}{\nu}} y \right] + A_{2n} \exp \left[ -\sqrt{\alpha_n^2 + \frac{iL^2 \omega}{\nu}} y \right] \right\}. \quad (9)$$

$$\begin{aligned} \hat{u}_{II}(y, z) = & B_0 \exp \left[ \sqrt{\frac{L^2 \omega}{2\nu}} (1+i)y \right] \\ & + C_0 \exp \left[ -\sqrt{\frac{L^2 \omega}{2\nu}} (1+i)y \right] \\ & + \sum_{n=1}^{\infty} \cos(n\pi z) \left\{ B_n \exp \left[ \sqrt{R} \left( \cos \frac{\phi}{2} + i \sin \frac{\phi}{2} \right) y \right] \right. \\ & \left. + C_n \exp \left[ -\sqrt{R} \left( \cos \frac{\phi}{2} + i \sin \frac{\phi}{2} \right) y \right] \right\}. \end{aligned} \quad (10)$$

$$\begin{aligned} \hat{u}_{III}(y, z) = & \sum_{n=1}^{\infty} D_n \cos(\alpha_n z) \left[ \exp \left( \sqrt{\alpha_n^2 + \frac{iL^2 \omega}{\nu}} y \right) \right. \\ & \left. - \exp \left( -\sqrt{\alpha_n^2 + \frac{iL^2 \omega}{\nu}} (y + 2b) \right) \right]. \end{aligned} \quad (11)$$

By eigenfunction expansions and matching the boundary condition between the regions I and II:

$$\hat{u}_{II} = \begin{cases} \hat{u}_I, & 0 \leq z < a, \\ 0, & a < z \leq L; \end{cases} \quad (12)$$

$$\frac{\partial \hat{u}_I(0, z, t)}{\partial y} = \frac{\partial \hat{u}_{II}(0, z, t)}{\partial y}, \quad (13)$$

and the interface between the two phases:

$$\hat{u}_I = \hat{u}_{III} \quad (14)$$

$$\frac{\partial \hat{u}_I(0, z, t)}{\partial y} = \mu_r \frac{\partial \hat{u}_{III}(0, z, t)}{\partial y}, \quad (15)$$

where  $\mu_r$  is the viscosity ratio  $\mu_r = \mu_{III}/\mu_I$ , one can get the analytical solution for each region. Then we define the transfer function to be the ratio between the energy spectrum at the interface (output) to the energy spectrum of the forcing (input):  $\mathcal{H} = \sqrt{\frac{\Phi(\omega)_{\text{output}}}{\Phi(\omega)_{\text{input}}}} = \hat{u}_I \hat{u}_I^*$ , where the forcing is applied at the top boundary of region II.

## COMPUTATIONAL SETUP

### Surface generation

The surface used in this study is manufactured at UT Dallas (courtesy Prof. Wonjae Choi), with a 3D surface profile measurement using a 20X objective lens obtained from MIT (courtesy Prof. Gareth McKinley). The sample is Aluminum 6061 sandblasted using 150 grit, etched for 25 seconds, boehmetized for 30 minutes and hydrophobized using Ultra Ever Dry top coat in isopropanol. The scanned surface data colored with height is illustrated in figure 2.

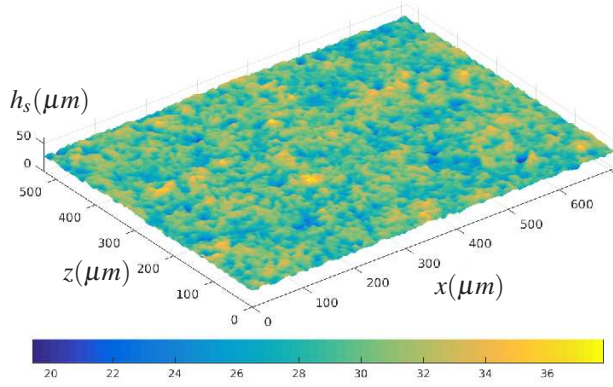


**Figure 2:** Illustration of the real rough surface. The contour legend describes the height of the surface profile.

We read the scanned surface data and use the number of pixels in the scan width and height as the number of nodes in the streamwise and spanwise directions respectively. The values of the roughness height and spatial location are then interpolated to cell centers of the discretized domain. Obstacle cells can only have one neighboring fluid cell; if this condition is not satisfied then the obstacle cell is removed and is assumed to be within the fluid domain. No-slip boundary conditions are applied at the edge cells and a weighted average of the neighboring cells is applied at the corners. This does not affect the pressure equation since we use collocated grids where the face-normal velocities are set to zero at the boundaries independent of the cell center value. This ensures a proper pressure jump recovery at the obstacle walls. The relevant statistics of the original surface are reported in table 1. Note that the surface has negative skewness indicating that the surface is mainly dominated by valleys instead of asperities.

**Table 1:** Statistics of the scanned surface used in the present work.

Parameter	Description	Value
$S_q$	RMS Roughness Height	$2.03 \mu\text{m}$
$S_v$	Maximum Valley Depth	$-10.0 \mu\text{m}$
$S_p$	Maximum Peak Height	$8.31 \mu\text{m}$
$S_{z,max}$	Maximum Peak to Valley Height	$18.38 \mu\text{m}$
$S_{z,5\times5}$	Mean Peak to Valley Height	$12.75 \mu\text{m}$
$S_{sk}$	Skewness	$-0.32$

## Problem description

Simulations are performed for a turbulent channel flow, where the rough surface is used on the bottom wall while the top wall remains flat. The domain extent is given by table 2.

**Table 2:** Case under consideration and the domain extents

Case	$L_x \times L_y \times L_z$
Turbulent channel	$2\pi\delta \times 2.13\delta \times \pi\delta$

Non-uniform grids are used in all the simulations with grid clustering near the surface region. Table 3 provides the grid resolution of the turbulent channel considered in this paper.

**Table 3:** Case under consideration, grid resolution and grid spacing in the wall-normal direction.

Case	$N_x \times N_y \times N_z$	$\Delta y_{min}^+$	$\Delta y_{max}^+$
Turbulent channel	$341 \times 128 \times 207$	1.8	6.12

The case names, domain definitions and interface heights are given in table 4.

**Table 4:** Cases considered, channel type, relevant  $Re_\tau$  and interface location for the turbulent channel flow problems.

Case	Channel flow condition	$Re_\tau$	Interface height $h$
1	Fully wetted flat	180	-
2	Fully wetted rough	180	$S_v$
3	Multiphase rough	180	0
4	Multiphase rough	180	$S_p$

No-slip boundary conditions are applied on both the top smooth wall and bottom rough wall with periodicity in the streamwise and spanwise directions. A constant body force in the liquid phase is applied such that the reference  $Re_\tau = 180$ . This was validated (not shown here) with the results of the flat smooth channel (Kim et al., 1987). The original surface is scaled such that  $S_q^+ \approx 1.6$ . The viscosity ratio of  $\mu_r = \mu_w/\mu_a = 1/50$  is used in all the simulations reported in this paper, where  $\mu_r$  is representative of an air-water interface which is assumed to be flat. Three cases were considered: (i) fully wetted rough channel for Case-2, (ii) two-phase rough channel with  $h/S_q = 0$  for Case-3, and (iii)  $h = S_p$  for Case-4. A flat smooth turbulent channel given by Case-1 serves as a baseline for comparison. Although in a realistic scenario the maximum interface height is

unphysical, it serves the purpose of providing the largest amount of slip that is theoretically achievable. It also helps describe the trend between limiting cases.

For the analytical solution, the height of the interface within the groove is shown figure 1. The parameters chosen are listed in table 5. An air-water interface is simulated and is extended in the parametric study to other viscosity ratios of liquid infused surfaces, and a range of geometry at different fluctuating frequencies representative of different  $Re_\tau$ .  $H/L$  is chosen to be representative of the location  $y^+ = 5$  of the viscous sublayer at the prescribed  $Re_\tau$ . The values of  $Re_\tau$  used in this work are representative of past studies on turbulent channel flows.

**Table 5:** Location of the forcing  $H$  and the interface  $h/b$ , the relevant non-dimensional number  $\frac{L^2\omega}{\nu}$ , the viscosity ratio  $\mu_r$  for all cases solved from analytical solution, and the applicable Reynolds numbers  $Re_\tau$ . For all cases,  $L/\delta = 18/3500$  is considered.

$H/L$	$h/b$	$\frac{L^2\omega}{\nu}$	$\mu_r$	$Re_\tau$
5.40	0.1 – 1.0	0.04 – 4.23	0.02, 0.37, 30.00	180
2.43	0.1 – 1.0	0.04 – 4.23	0.02, 0.37, 30.00	400
1.65	0.1 – 1.0	0.04 – 4.23	0.02, 0.37, 30.00	590

## RESULTS AND DISCUSSION

### Turbulent channel flow

We simulate the turbulent channel flow, the cases are run until a statistically stationary solution is obtained to evaluate the relevant mean profiles and turbulence intensities.

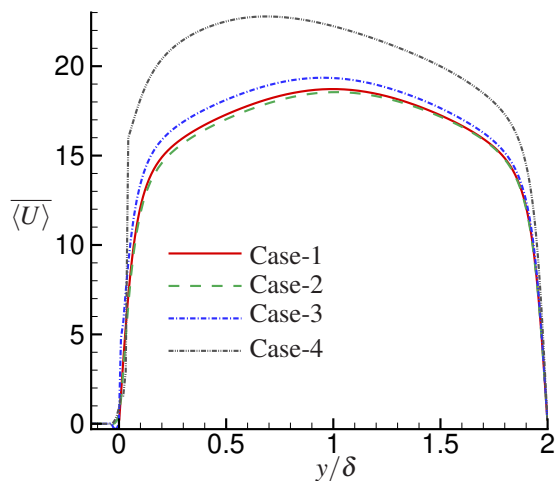


**Figure 3:** Mean profile of the bulk velocity normalized with the average friction velocity  $u_\tau$ .

Mean velocity profiles and Reynolds stresses are computed for Cases (1-4). The mean velocity profile normalized by the friction velocity  $u_\tau$  of the baseline Case-1 is shown in figure 3. The fully wetted simulation given by Case-2 shows a slightly lower centerline mean velocity  $\langle U \rangle$  with a slight shift away from the rough wall when compared to Case-1. This is not very evident near the wall but is more evident in the channel centerline. The mean roughness height is hydrodynamically smooth,  $S_q^+ \approx 1.6$ , which explains the small difference observed. It is known however that a hydrodynamically smooth channel does not show any difference. Using the surface property  $S_{z5 \times 5}^+ \approx 11$ , which is reported by Busse et al. (2017) to be a more suitable equivalent to the sand-grain roughness  $k$ , it is possible to explain why we see a difference. The value is larger than 5 hence can be considered in the early transition from hydrodynamically smooth to rough regime. The presence of an air-water interface displays a clear evidence of slip due to the interface. Cases 3 and 4 clearly show a slip effect in  $\langle U \rangle$ .

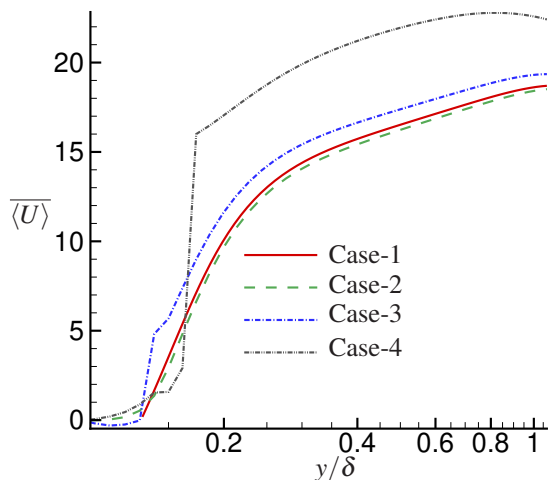


**Figure 4:** Mean profile of the bulk velocity normalized with the average friction velocity  $u_\tau$  on a semilog scale.

Figure 4 shows the mean profile plotted on a semilog scale to look at the near wall behavior. Cases-3 exhibits a reverse flow in the near wall region, and at the centerline location there is a clear increase in maximum velocity for both cases 3 and 4. Case-4 shows the largest slip due to the maximum slip area exposed to the liquid. The linear region of the mean profile seems to be suppressed due to the presence of the interface. As observed in Case-3 there exists a linear increase in the velocity profile from the wall towards the interface location where a slight gradient is present. The slope in the liquid phase is close to that of Case-1 however

the region of linearity is smaller. In case-4 the linear region is almost non-existent in the liquid phase and a sharp gradient is present in the air phase. The  $\langle U \rangle$  profile is partially skewed towards the region of the wall roughness due to the slip effect. This indicates that the high momentum fluid is moving closer to the bottom wall. The skewness in the mean velocity profile for Case-4 is more pronounced when compared to cases 1-3, the skewness also affects the maximum velocity which is also shifted from the center towards the rough wall region.

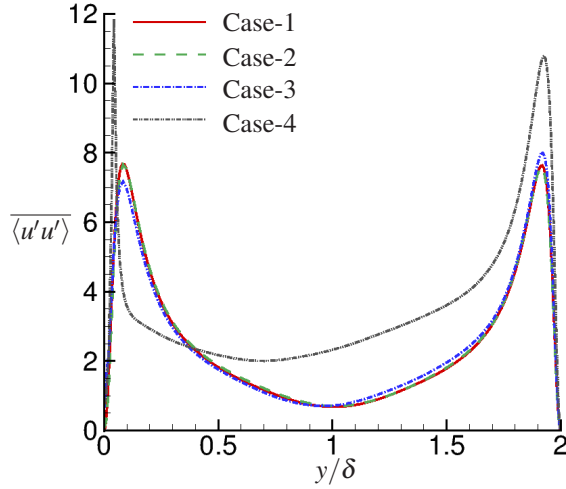


**Figure 5:** Components of Reynolds stress tensor normalized with the average friction velocity  $u_\tau^2$  of Case 1.

Figure 5 shows the turbulence intensities in the streamwise direction  $\langle u'u' \rangle$  for cases 1-4. Comparing cases 1 and 2, the plot does not show much difference at the peak. The bottom rough wall is almost equivalent to the smooth wall, the top flat wall however does show a difference in a slightly smaller peak than that of the baseline Case-1 by almost 1%. As we move away from the wall, the streamwise turbulence intensity increases when compared to the baseline. For Case-3 the interface is introduced at the root-mean-square (rms) height of the roughness. We observe a clear drop in the peak stress near the rough wall region, and an increase in peak stress near the top smooth wall. There is a slight skew of the minimum stress values towards the rough wall region away from the centerline of the channel. For Case-4 where the interface is at the maximum peak of the roughness, the streamwise turbulence intensity is much higher when compared to the baseline peak value. The top smooth flat wall region has a lower peak when compared to the rough wall region ( due to momentum balance given a constant body force). The skewness of the centerline

value is also pronounced in this case, with the values shifting towards the highest slip region near the rough wall.

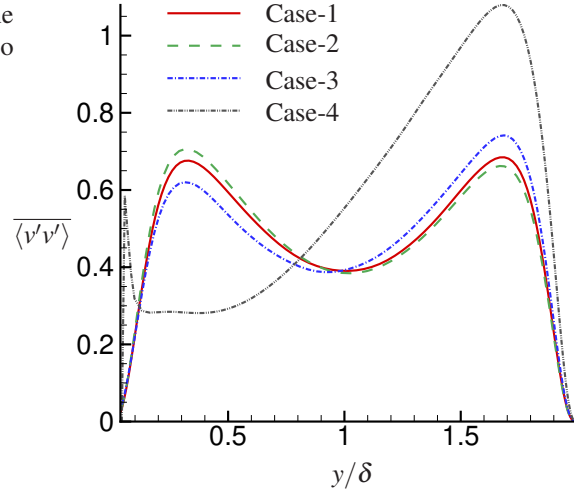


**Figure 6:** Components of Reynolds stress tensor normalized with the average friction velocity  $u_\tau^2$  of Case 1.

Figure 6 shows the wall-normal turbulence intensity  $\langle v'v' \rangle$ . Comparing the baseline Case-1 to Case-2, a higher peak near the bottom rough wall is observed while a lower peak near the top flat wall is obtained. The centerline value is equivalent in both cases. In Case-3 a fluid interface is introduced, the peak value in turbulence intensity near the rough wall region decreases while the reverse happens near the top flat wall region. The minimum value of the wall-normal turbulence intensity skews towards the bottom rough wall region away from the centerline of the channel. For Case-4 the interface is located at the height of the maximum asperity of the rough surface. The wall-normal turbulence intensity peak in the rough wall region is reduced significantly. There is an increase in the wall-normal stress within the air region, it then goes to zero at the interface, peaks then starts decreasing again as we move away from the wall since we enforce a zero wall-normal velocity at the interface. The centerline is significantly skewed towards the rough wall region. The turbulence intensities go to a larger peak at the top flat wall region to balance out the constant body force. Case-4 does not show the same smooth transition behavior in turbulence intensity in near wall regions to the channel centerline when compared to all the other cases 1-3.

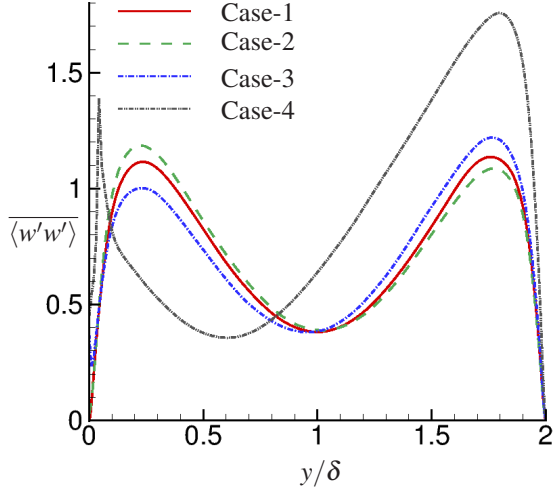


**Figure 7:** Components of Reynolds stress tensor normalized with the average friction velocity  $u_\tau^2$  of Case 1.

The spanwise turbulence intensity  $\overline{w'w'}$  exhibit a similar behavior as the wall-normal turbulence intensity with the exception of Case-4 as seen in figure 7. Case-2 has a higher peak stress in the near rough wall region, the constant pressure gradient balances out at the flat top wall where we observe a lower peak in stress. This is reversed in Case-3 where the peak is suppressed near the rough wall, and enhanced in the top wall region. However in Case-4, the peak at the rough wall region is not further suppressed. The peak in the top wall region behaves as expected and is significantly higher than cases 1-3.

The Reynolds stresses  $\overline{u'v'}$  is shown in figure 8. Case-2 has a lower peak in near the rough wall when compared to Case-1. This is due to the increase in the vertical velocity fluctuations which enhances the mixing mechanism near the rough surface. Near the top wall, the behavior of Case-2 and Case-1 follow the same trend. The peak value of the Reynolds stresses remains lower in Case-2 when compared to the Case-1. Once an interface is introduced in Case-3, we get the opposite effect. This is evident in both cases (3 and 4) where an interface is placed at  $h = 0$  or  $h = S_p$ . The Reynolds stress value near the wall for cases 3 and 4 has a higher peak when compared to both cases 1 and 2. When the interface is at  $h = S_p$ , the peak of Reynolds stress is highest when compared to all the other cases. An oscillation in the stress values is observed at the location of the interface due to the imposed boundary condition which enforces a zero wall-normal velocity to satisfy the infinite surface tension condition. It is therefore evident that there are competing effects between the interface suppressing vertical velocity fluctuations and the asperities doing the opposite by enhancing them.

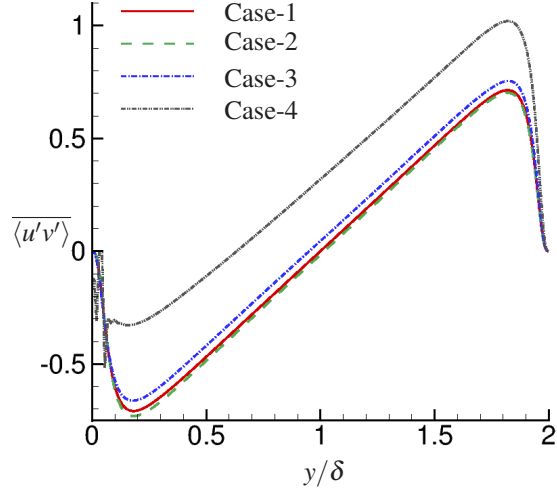


**Figure 8:** Components of Reynolds stress tensor normalized with the average friction velocity  $u_\tau^2$  of Case 1.

#### Unsteady multiphase Stokes solution

The analytical solution of the transfer function is validated against VOF simulations over a range of frequencies. The domain of the VOF simulations is equivalent to that of the analytic solution, the boundary conditions of region II and the VOF simulation are periodic. There is an exception to the applied boundary condition at the interface, where the analytic solution explicitly applies equal velocities and shear stress as shown in eq. 14 and 15 but in the VOF simulation it is handled implicitly where the infinite surface tension keeps the interface flat. Good agreement is seen in figure 9. The frequency range is selected such that it is representative of a turbulent channel flow at a given  $Re_\tau$  listed on the last column in table 5.

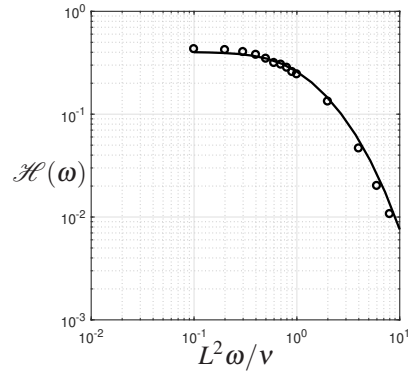


**Figure 9:** Comparison of the transfer function results from VOF (symbols) with analytical solutions (solid line).  $L = 1$ ,  $\nu = 1$ ,  $H = 2.5$ ,  $b = h = 1.75$ , and  $\mu_r = 0.02$ .

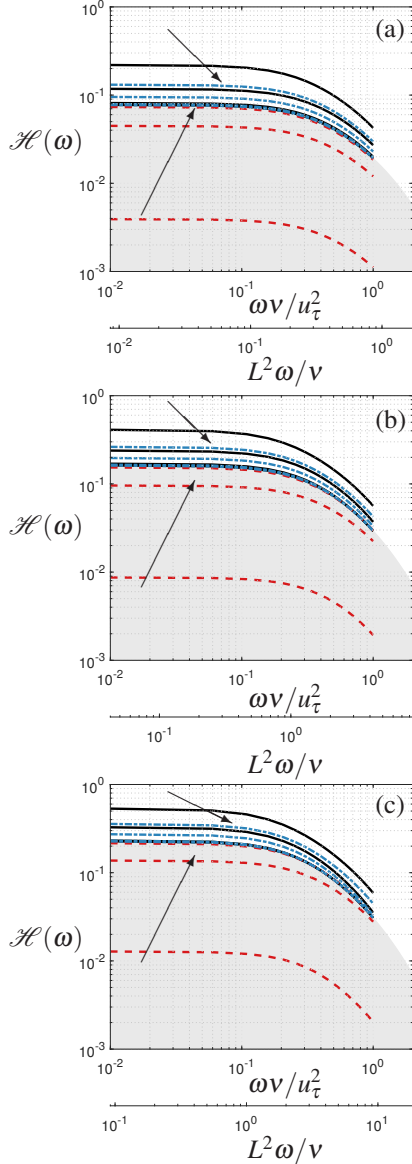


**Figure 10:** Transfer function  $\mathcal{H}(\omega)$  with increasing forcing frequency  $\omega$  normalized by either viscous units  $u_\tau^2/v$  (top axis) or modeled equation units  $v/L^2$  (bottom axis) with increasing representative (a)  $Re_\tau = 180$ , (b)  $Re_\tau = 400$ , (c)  $Re_\tau = 590$ . Here,  $\mu_r = 0.02, 0.37, 30.00$  is denoted by black solid lines, blue dashed-dotted lines, and red dashed lines respectively.  $\mathcal{H}(\omega)$  solutions with  $\mu_r > 1$  are shaded in gray. The arrows indicate decreasing  $h/b$  in the area of  $\mu_r > 1$  or  $\mu_r < 1$ . As  $h/b$  decreases, penetration of outside fluid grows,  $\mathcal{H}(\omega)$  merges towards the border between the gray and white areas ( $\mu_r = 1$ ).

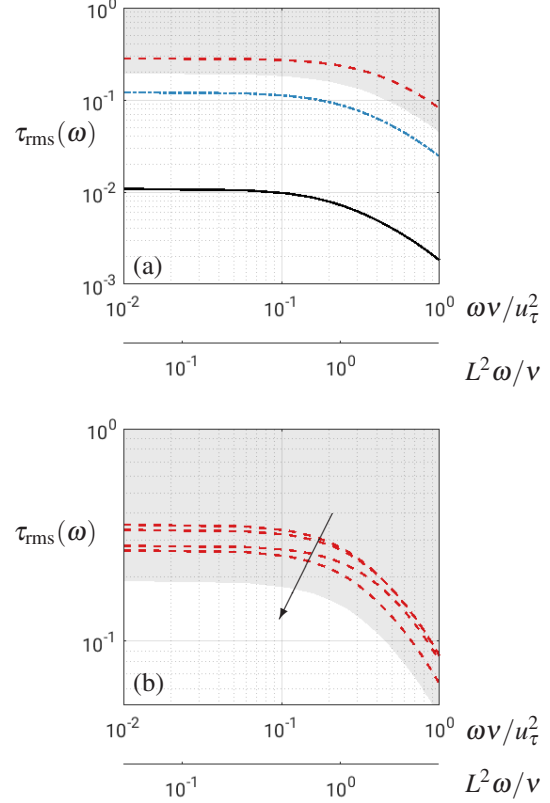


**Figure 11:** Shear stress  $\tau_{\text{rms}}(\omega)$  at the interface between regions I and III with increasing forcing frequency  $\omega$  normalized by either viscous units  $u_\tau^2/v$  (top axis) or modeled equation units  $v/L^2$  (bottom axis) with representative Reynolds number  $Re_\tau = 400$ . (a) Penetration rate is  $h/b = 0$ ; viscosity ratios are  $\mu_r = 30$  (long-dashed line),  $\mu_r = 0.37$  (short dashed line), and  $\mu_r = 0.02$  (solid line). (b) Viscosity ratio is  $\mu_r = 30$ ; penetration rates are  $h/b = 0, 0.15, 0.5, 0.9$ . Arrow indicates the increasing of penetration rate.

The location of the forcing  $H$  is equivalent to  $y^+ = 5$  for the  $Re_\tau$  given. The viscosity ratios are chosen to be 0.02, 0.37, 30.00 to represent air, heptane, and Dupont Krytox to water respectively (Rosenberg et al., 2016). Results of the parametric study for the transfer function are shown in figure 10. Overall, high frequency suppresses the forcing energy at the interface. However, one must bear in mind that as Reynolds number increases, the forcing also comes closer to the surface. The shaded area represents the condition  $\mu_r > 1$ . The trend of  $\mathcal{H}$  differs between  $\mu_r > 1$  and  $\mu_r < 1$ . When  $\mu_r > 1$ , as  $h/b$  decreases, the penetration of the outside fluid improves the transfer of forcing. The opposite is true when  $\mu_r < 1$ . Moreover, neither of these two conditions cross the border that represents  $\mu_r = 1$ . The air-water interface still performs the best over the other two types of

combinations, which is intuitively reasonable, considering that the interface does not break or drain. Figure 11 shows the trend of the shear stress with respect to increasing frequency at a representative Reynolds number of  $Re_\tau = 400$ . Similar to the trend of the transfer function: the larger the viscosity ratio, the larger the shear stress at the interface; when the fluid inside the groove is more viscous, penetration of the outside fluid reduces shear stress.

## SUMMARY

DNS of turbulent channel flow at  $Re_\tau = 180$  is performed, where the bottom wall is a realistically rough SHS. Simulations are also performed for a smooth wall to serve as a baseline. The fully wetted case and an air-water interface at various heights are compared to the smooth channel. The effect of roughness and interface heights are discussed in detail. An analytical model based on a unsteady multiphase Stokes flow over an idealized grooves is presented. A parametric study is conducted for a range of geometry, frequency oscillations and viscosity ratios.

Simulations of a fully wetted rough case and two interface heights  $h = 0$  and  $h = S_p$  are performed. The mean velocity profile  $\langle U \rangle$  shows a small overall decrease in the fully wetted case due to roughness, whereas the presence of an interface shows an increase (up to 27%) in  $\langle U \rangle$ . The fully wetted case shows an increase in shear at the bottom rough wall and decreases at the top wall since a constant body force is prescribed. The streamwise  $\langle u'u' \rangle$ , wall-normal  $\langle v'v' \rangle$  and spanwise  $\langle w'w' \rangle$  turbulence intensities, show an increase in peak value for the fully wetted roughness and a suppression in peak values with the presence of an interface. The Reynolds shear stress  $\langle u'v' \rangle$  increases in peak intensity for the fully wetted rough wall case which is indicative of enhanced mixing. When the interface is present, the shear stress is further suppressed. The peak in mean velocity, turbulence intensities and Reynolds shear stress shift towards the slip wall. This indicates a shift in high momentum fluid towards the rough wall with increasing slip. Overall there exists a competing effect between the interface suppressing vertical fluctuations and the exposed asperities of the rough surface enhancing them.

Based on the observation that the mean Reynolds stresses are low near the SHS, the near field of the surface is modeled as a Stokes flow driven by a oscillating streamwise velocity in the vicinity of longitudinal grooves and solved analytically. The solution shows good agreement with VOF simulation of the same modeled problem. A parametric study was conducted by varying the frequency of the forcing function, the representative Reynolds number, the location of the

interface (penetration rate), and the viscosity ratio across the interface. It is found that the larger the frequency, the harder it is for the forcing to be transferred to the surface; increasing  $Re_\tau$  can increase the transfer function; the viscosity ratio combined with penetration rate shows opposite effect on the shear stress when switching from  $> 1$  to  $< 1$ : when  $\mu_r < 1$ , penetration of the outside fluid will prohibit the transfer of energy from outside; when  $\mu_r > 1$ , penetration of the outside fluid will help the transfer of outside energy.

## ACKNOWLEDGEMENTS

This work was supported by the United States Office of Naval Research (ONR) MURI (Multidisciplinary University Research Initiatives) program under Grant N00014-12-1-0874 managed by Dr. Ki-Han Kim. Computing resources were provided by the Minnesota Supercomputing Institute (MSI). We are grateful to Prof. W. Choi at University of Texas Dallas and Prof. G. H. McKinley at MIT for providing us with the scanned surface data used in the present work. The authors would like to thank Dr. P. Kumar for the helpful discussions and suggestions.

## REFERENCES

- Belyaev, A. V. and Vinogradova, O. I. “Effective slip in pressure-driven flow past super-hydrophobic stripes”. *J. Fluid Mech.*, 645:489–499, 2010.
- Brackbill, J. U., Kothe, D. B., and Zemach, C. “A continuum method for modeling surface tension”. *J. Comput. Phys.*, 100(2):335–354, 1992.
- Busse, A., Thakkar, M., and Sandham, N. D. “Reynolds-number dependence of the near-wall flow over irregular rough surfaces”. *J. Fluid Mech.*, 810: 196–224, 2017.
- Cassie, A. B. D. and Baxter, S. “Wettability of porous surfaces”. *Trans. Faraday Soc.*, 40:546–551, 1944.
- Choi, C. H. and Kim, C. J. “Large slip of aqueous liquid flow over a nanoengineered superhydrophobic surface”. *Phys. Rev. Lett.*, 96:066001, 2006.
- Cottin-Bizonne, C., Barrat, J. L., Bocquet, L., and Charlaix, É. “Low-friction flows of liquid at nanopatterned interfaces”. *Nat. Mater.*, 2(4):237–240, 2003.
- Cummins, S. J., Francois, M. M., and Kothe, D. B. “Estimating curvature from volume fractions”. *Computers & Structures*, 83(6):425–434, 2005.
- Emami, B., Tafreshi, H. V., Gad-el Hak, M., and Tepper, G. C. “Predicting shape and stability of air-water

- interface on superhydrophobic surfaces with randomly distributed, dissimilar posts”. Applied Physics Letters, 98(20):203106–203106, 2011.
- Joseph, P., Cottin-Bizonne, C., Benoit, J.-M., Ybert, C., Journet, C., Tabeling, P., and Bocquet, L. “Slippage of water past superhydrophobic carbon nanotube forests in microchannels”. Phys. Rev. Lett., 97:1–4, 2006.
- Kim, J., Moin, P., and Moser, R. “Turbulence statistics in fully developed channel flow at low Reynolds number”. J. Fluid Mech., 177:133–166, 1987.
- Lauga, E. and Stone, H. A. “Effective slip in pressure-driven stokes flow”. J. Fluid Mech., 489: 55–77, 7 2003.
- Li, Y., Alame, K., and Mahesh, K. “Feature resolved simulations of turbulence over superhydrophobic surfaces”. In Proceedings of the 31st Symposium on Naval Hydrodynamics, Monterey, USA, 2016.
- Li, Y., Alame, K., and Mahesh, K. “Feature-resolved computational and analytical study of laminar drag reduction by superhydrophobic surface”. Phys. Rev. Fluids, 2:054002, 2017.
- Mahesh, K., Constantinescu, G., and Moin, P. “A numerical method for large-eddy simulation in complex geometries”. J. Comput. Phys., 197(1):215, 2004.
- Maynes, D., Jeffs, K., Woolford, B., and Webb, B. W. “Laminar flow in microchannel with hydrophobic surface patterned microribs oriented parallel to the flow direction”. Phys. Fluids, 19:093603, 2007.
- Nizkaya, T. V., Asmolov, E. S., and Vinogradova, O. I. “Gas cushion model and hydrodynamic boundary conditions for superhydrophobic textures”. Phys. Rev. E, 90:043017, 2014.
- Ou, J. and Rothstein, J. P. “Direct velocity measurements of the flow past drag-reducing ultrahydrophobic surfaces”. Phys. Fluids, 17:103606, 2005.
- Ou, J., Perot, B., and Rothstein, J. P. “Laminar drag reduction in microchannels using ultrahydrophobic surfaces”. Phys. Fluids, 16:4635–4643, 2004.
- Rosenberg, B. J., Van Buren, T., Fu, M. K., and Smits, A. J. “Turbulent drag reduction over air- and liquid-impregnated surfaces”. Phys. Fluids, 28(1), 2016.
- Sbragaglia, M. and Prosperetti, A. “A note on the effective slip properties for microchannel flows with ultrahydrophobic surfaces”. Phys. Fluids, 19(4), 2007.
- Scardovelli, R. and Zaleski, S. “Analytical relations connecting linear interfaces and volume fractions in rectangular grids”. J. Comput. Phys., 164(1):228–237, 2000.
- Seo, J. and Mani, A. “On the scaling of the slip velocity in turbulent flows over superhydrophobic surfaces”. Phys. Fluids, 28(2), 2016.
- Vinogradova, O. I. “Drainage of a thin liquid film confined between hydrophobic surfaces”. Langmuir, 11:2213–2220, 1995.
- Wang, L. P., Teo, C. J., and Khoo, B. C. “Effects of interface deformation on flow through microtubes containing superhydrophobic surfaces with longitudinal ribs and grooves”. Microfluid Nanofluidics, 16:225–236, 2014.
- Wenzel, R. N. “Resistance of solid surfaces to wetting by water”. Ind. Eng. Chem., 28(8):988–994, 1936.
- Woolford, B., Prince, J., Maynes, D., and Webb, B. W. “Particle image velocimetry characterization of turbulent channel flow with rib patterned superhydrophobic walls”. Phys. Fluids, 21(8): 085106, 2009.
- Ybert, C., Barentin, C., Cottin-Bizonne, C., Joseph, P., and Bocquet, L. “Achieving large slip with superhydrophobic surfaces: Scaling laws for generic geometries”. Phys. Fluids, 19:123601, 2007.